TÜBİTAK

Turkish Journal of Earth Sciences

http://journals.tubitak.gov.tr/earth/

Research Article

Turkish J Earth Sci
(2020) 29: 434-454

doi:10.3906/yer-1909-2

Seismic identification of gas hydrates: a case study from Sakarya Canyon, western Black Sea

Aslıhan NASIF[1,2,*], Faik Erdeniz ÖZEL[1], Derman DONDURUR[1]

[1]Institute of Marine Sciences and Technology, Dokuz Eylül University, İnciraltı, İzmir, Turkey

[2]Natural and Applied Sciences Institute, Dokuz Eylül University, Buca, İzmir, Turkey

Received: 02.09.2019 • **Accepted/Published Online:** 24.12.2019 • **Final Version:** 16.03.2020

Abstract: Multichannel seismic, 3.5-kHz Chirp subbottom profiler and multibeam bathymetric data were collected along the western Black Sea margin, offshore Sakarya River, to investigate the bottom-simulating reflections (BSRs), free gas accumulations, and mud volcanoes. Geometries from the seismic data indicate widespread BSRs along the continental rise between 750 and 1950 m water depths, 70 to 350 ms below the seafloor. Seismic attribute analyses have been applied to the seismic data to reveal the acoustic properties of the gas hydrates. According to the results from such analyses, we conclude that there are acoustically transparent zones beneath most of the BSRs in the area, which are interpreted as free gas accumulations, and the gas hydrate-bearing sediments are acting as seals for the free gas in the underlying sediments. Stability analysis of the gas hydrates from different BSR zones in the area suggests that the gas composition in the gas hydrates may change locally. As we do not have ground truth data from BSR zones, the exact composition of the gas forming the gas hydrates is unknown. However, hydrocarbon productivity of the area, chromatography results of the shallow sediment samples nearby, and stability analysis of the gas hydrates indicate the possible existence of a thermogenic gas component in the gas hydrate composition, resulting in a mixture of gas hydrates.

Key words: Gas hydrates, bottom-simulating reflections, seismic attributes, gas-charged sediments, mud volcanoes

1. Introduction

Gas hydrates are crystalline solids formed of water and gas, and they naturally occur within shallow subsurface sediments at the continental margins with water depths typically exceeding 500 m. They can be stable in solid hydrate phase only in high-pressure and low-temperature conditions known as thermobaric stability conditions (Sloan, 1990; Ginsburg and Soloviev, 1997; Milkov and Sassen, 2002). Water molecules act as cages for gas molecules, in which different types of gases are trapped. Though the hydrate-forming gas is commonly methane, different gas compositions and even a mixture of heavy hydrocarbons as well as nonhydrocarbon gases, such as CO_2 and H_2S, can be found within the hydrate-bearing structure (Kvenvolden, 1993; Milkov and Sassen, 2002). Studying the gas hydrates is primarily important because:

· gas hydrates can be considered as a future energy source since they contain huge amounts of hydrocarbon gases in hydrate form,

· gas hydrates can act as seals by trapping the free gas accumulating in the underlying sediments,

· it may indicate the existence of deeper thermogenic reservoirs when heavy hydrocarbon gases are involved in the hydrate structure,

· rapid dissociation of gas hydrates may cause massive submarine slumps, which ultimately gives rise to destructive tsunamis,

· their identification in advance is essential in well design and site selection as gas hydrates and underlying free gas are considered as shallow hazards in drilling operations,

· large amounts of gas hydrate dissociations may have a negative effect on the climate since methane is a greenhouse gas.

Bottom-simulating reflections (BSRs) in seismic sections coinciding with the base of the gas hydrate stability zone (BGHZ) are considered as one of the most prominent indications of subsurface gas hydrate occurrence (Kvenvolden et al., 1993; Andreassen et al., 1997). They determine the phase boundary between the hydrate in the gas hydrate stability zone (GHZ) and free gas in the underlying sediments. The BGHZ (or BSR) follows the isotherms since the stability of the gas hydrates

* Correspondence: aslihan.nasif@deu.edu.tr

primarily depends on temperature distribution, and hence on geothermal gradient, for constant pressure conditions.

Specific characteristics of BSRs can be listed as follows:

· BSRs often crosscut the reflections from the normal subsurface stratigraphy since they follow the isothermal levels and therefore generally mimic the seafloor.

· BSRs are typically characterized by opposite polarity reflections with respect to the seafloor reflection, indicating a velocity decrease below the BSR level assuming a constant density medium.

· The amplitudes of BSRs are generally high with respect to the surrounding reflections. They often produce bright amplitudes on the amplitude envelope sections.

· Depth of the BSRs from the seafloor and hence the thickness of the GHZ generally increase with increasing water depth.

Complex trace seismic attribute analysis is a useful tool to analyze the free gas and gas hydrate accumulations as it can reveal the seismic imprints of these structures because of the above-mentioned characteristics of the gas hydrates and underlying free gas (e.g., Taylor et al., 2000; Coren et al., 2001; Satyavani et al., 2008; Lee et al., 2017; Kumar et al., 2019).

In the last two decades, several studies have been performed in the Black Sea indicating shallow gas accumulations, oil and gas seeps, and existence of mud volcanoes (Ivanov et al., 1996; Limonov et al., 1997; Okyar and Ediger, 1999; Amouroux et al., 2002; Dimitrov, 2002; Ergün et al., 2002; Bohrmann et al., 2003; Lüdmann et al., 2004; Klaucke et al., 2006; Sahling et al., 2009; Naudts et al., 2009; Pape et al., 2011; Römer et al., 2012; Dondurur et al., 2013; Körber et al., 2014). Menlikli et al. (2009) showed the potential hydrocarbon resources of the Turkish Black Sea. The study area lies approximately 25 km west of the Akçakoca field where Turkish Petroleum has been producing dry gas with a biogenic to mixed origin (Menlikli et al., 2009).

Gas hydrate studies in the Black Sea date back to the late 1980s (Nomokonov and Stupak, 1988; Korsakov et al., 1989). During Training Through Research expeditions in the 1990s, gas hydrates were sampled over some mud volcanoes in the deep waters of the central Black Sea (Ivanov et al., 1996) and in the Sorokhin Trough (Ivanov and Woodside, 1996; Woodside et al., 1997). Woodside et al. (2003) interpreted high-amplitude reflections observed from 5-kHz subbottom profiler records from the central Black Sea basin as thin gas hydrate layers. Lüdmann et al. (2004) reported the first BSR along the Dnieper Canyon, and then Zillmer et al. (2005) investigated this BSR using ocean bottom seismometer data to quantify the gas hydrate and free gas saturations and suggested a 100-m-thick free gas beneath the BSR level. Popescu et al. (2006) showed the first multiple BSRs along the levees of the Danube Canyon in the NW Black Sea.

Following these initial observations, several studies have been conducted especially in the central and NW Black Sea to delineate and analyze the BSRs and gas hydrates. Römer et al. (2012) used an autonomous underwater vehicle to map the gas hydrate "mounds" in the surficial sediments and sampled gas hydrates in the Kerch seep area in the northern Black Sea margin. Minshull and Keddie (2010) mapped the BSR distribution using a 3D seismic dataset and calculated the geothermal gradients for offshore Batumi in the eastern Black Sea, and Pape et al. (2011) sampled the gas hydrates and analyzed the gas concentrations for the same area. Hillman et al. (2018) investigated the Danube Fan using P-cable 3D seismic data and suggested that the BSR was not in equilibrium with the present-day topography of the canyon system, while Zander et al. (2018) investigated the impacts of gas hydrate exploitation on the slope stability for the same area. Despite these different investigations, studies on the gas hydrates along the whole Turkish Black Sea margin are very poor and only one study from the western margin has been published so far. Dondurur et al. (2013) reported a possible connection between gas hydrate dissociation and massive slope failures in the continental rise, offshore Zonguldak, western Black Sea.

Studies on estimating the total methane trapped within the gas hydrates in the Black Sea sediments are very limited and the results are controversial. Using a finite element modeling approach, Parlaktuna and Erdoğmuş (2001) suggested 6.89–9.66 × 10^{13} m^3 gas for the central deep basin. Klauda and Sandler (2003) suggested 0.85 × 10^{15} m^3 methane for the Black Sea basin while Vassilev and Dimitrov (2002) calculated 10 to 50 × 10^{12} m^3. For an average sand content of 14.75%, Merey and Sinayuç (2016) calculated 13.6 × 10^{12} m^3 methane in the hydrate phase for the whole basin considering a 303-m-thick GHZ.

The main purpose of this study is to map the distribution and depth of the BSRs and analyze the free gas associated with the sediments below the BSRs as well as mud volcanoes in the continental rise of the Sakarya Canyon, offshore Karasu, western Black Sea margin. This is the first study in the area, which defines the distribution, acoustic properties, and stability conditions of the gas hydrates using multichannel seismic (MCS) and 3.5-kHz Chirp subbottom profiler data. Complex trace attribute analyses are also performed on the MCS data to obtain acoustic properties of the BSRs, gas-charged sediments, and mud volcanoes.

2. Geological and oceanographic settings

The Black Sea is considered as a back-arc basin generated by the northward subducting Tethys Ocean (Okay et al., 1994; Robinson et al., 1996; Spadini et al., 1996). It comprises western (WBS) and eastern (EBS) subbasins separated by a regional high, the mid-Black Sea high,

which is subdivided into two ridges named Andrusov and Archangelsky to the north and south, respectively (Figure 1a). The Black Sea has an extensional origin; however, the tectonic setting changed to a compressional regime during the Eocene, and its margins are currently characterized by a compressive deformation (Tarı et al., 2000) (Figure 1a).

Two different ideas exist about the opening of both basins. Some researchers (Zonenshain and Le Pichon, 1986; Finetti et al., 1988; Okay et al., 1994) suggested that the WBS and EBS were simultaneously opened by the rifting of the western and central Pontides from the Moesian Platform in the Late Cretaceous. According to Spadini et al. (1996) and Robinson et al. (1995, 1996), however, the WBS and EBS have separate origins with different rifting histories. They suggested that the WBS basin was opened by the rifting of the western and central Pontides from the Moesian Platform in the middle Barremian while the EBS was opened by the clockwise rotation of the Andrussov Ridge during the Middle Paleocene to Eocene.

A very narrow continental shelf and a steep continental slope exist along the eastern and southern margins. The WBS basin is floored by an oceanic crust and the postrift sediment thickness since the Upper Cretaceous reaches approx. 13 km in the central basin (Finetti et al., 1988). Robinson et al. (1996) indicated that the narrowed continental shelf of the western Black Sea Turkish WBS margin involves the northern extension of the Pontides thrust belt, which forms prospective compressional anticlines close to the shore.

The only connection of the Black Sea with the Mediterranean for water exchange is through the narrow Bosphorus and Dardanelles straits. Present-day oceanographic conditions of the Black Sea are characterized by an oxic-anoxic interface lying at a water depth of approx. 150 m, and the water temperature in the deep basin is quite stable at 9 °C (Murray et al., 2007). Several researchers suggested that the sea level of the Black Sea was 120 m lower than the present-day sea level during the last glacial maximum (e.g., Panin and Popescu, 2007; Lericolais et al., 2009; Yanchilina et al., 2017), and the Black Sea was an enclosed lake with the exposed continental shelves open to subaerial erosion (Ryan et al., 1997; Panin and Popescu, 2007; Lericolais et al., 2009; Yanchilina et al., 2017).

The Turkish WBS continental margin has the common morphological characteristics of a modern ocean margin with a narrow shelf (up to 10 km wide), a steep continental slope (with inclinations exceeding 25°) carved by canyon systems, a continental rise with gentle slopes, and a smooth abyssal plain with a maximum water depth of 2200 m (Dondurur et al., 2013; Nasıf and Dondurur, 2017; Sipahioğlu and Batı, 2017; Nasıf et al., 2018). The continental rise can be considered as the main depocenter for the terrigenous sediments transported by the canyon systems (Dondurur and Çifçi, 2007; Dondurur et al., 2013). The heat flow values of both Black Sea basins are low, and minimal heat flow values (<30 mW/m^2) are observed in the central part of the basin (Kutas et al., 1998). Using several heat flow measurements and thermal conductivity values, Vassilev and Dimitrov (2002) suggested a geothermal gradient value of approximately 50 °C/km for our study area. According to the Global Heat Flow Database (www.heatflow.org), there are two heat flow measurements (53 and 58 °C) close to the NE border of our study area (Figure 1b). Based on these values we estimate the geothermal gradient in the study area to be between 50 and 60 °C/km.

Recently, Dondurur et al. (2013) investigated the WBS margin using MCS data and they reported widespread sediment erosion on different scales along the continental slope and rise. They proposed that the large slides in the area were triggered by excess pore pressures in shallow sediments due to the fluid flow produced from dissociation of deeper gas hydrate layers, in addition to the seismicity of the North Anatolian Fault.

The study area is located in front of a large river called the Sakarya River (Figure 1b) in the WBS margin comprising a total area of approx. 3300 km^2. The area is deeply eroded by a canyon system known as the Sakarya Canyon (SC), which can be traced from shelf break to deep basin in the bathymetric data (Figure 1b).

3. Datasets and methods

During two research cruises in 2012 and 2016, 2D MCS, Chirp subbottom profiler, and multibeam bathymetric data were acquired simultaneously over the SC aboard the *R/V K. Piri Reis* of the Institute of Marine Sciences and Technology, Dokuz Eylül University. Figure 1b shows the locations of the acquired seismic lines.

A 168-channel, 1050-m-long digital streamer and a 45+45 in^3 generator-injector (GI) gun were used to collect approx. 1400 km of MCS data. Tow depths for the streamer and GI gun were 4 and 3 m, respectively. The record length, sampling, and shot intervals were 6 s, 1 ms, and 25 m, respectively, resulting in 21-fold high-resolution MCS data. Processing of the MCS data included data loading, geometry definition, band-pass filtering (8 to 180 Hz), trace editing, f-k dip filtering, surface-related multiple elimination (SRME), sort to CDP gathers, velocity analysis (approx. every 1000 m along the lines), normal move-out correction, stacking, poststack time migration, and spherical divergence correction. Since the analyses are based on the relative amplitude information embedded in the MCS data, only true amplitude seismic data were displayed and analyzed.

A hul-mounted SeaBeam 1050D multibeam bathymetric system was used to collect bathymetric data.

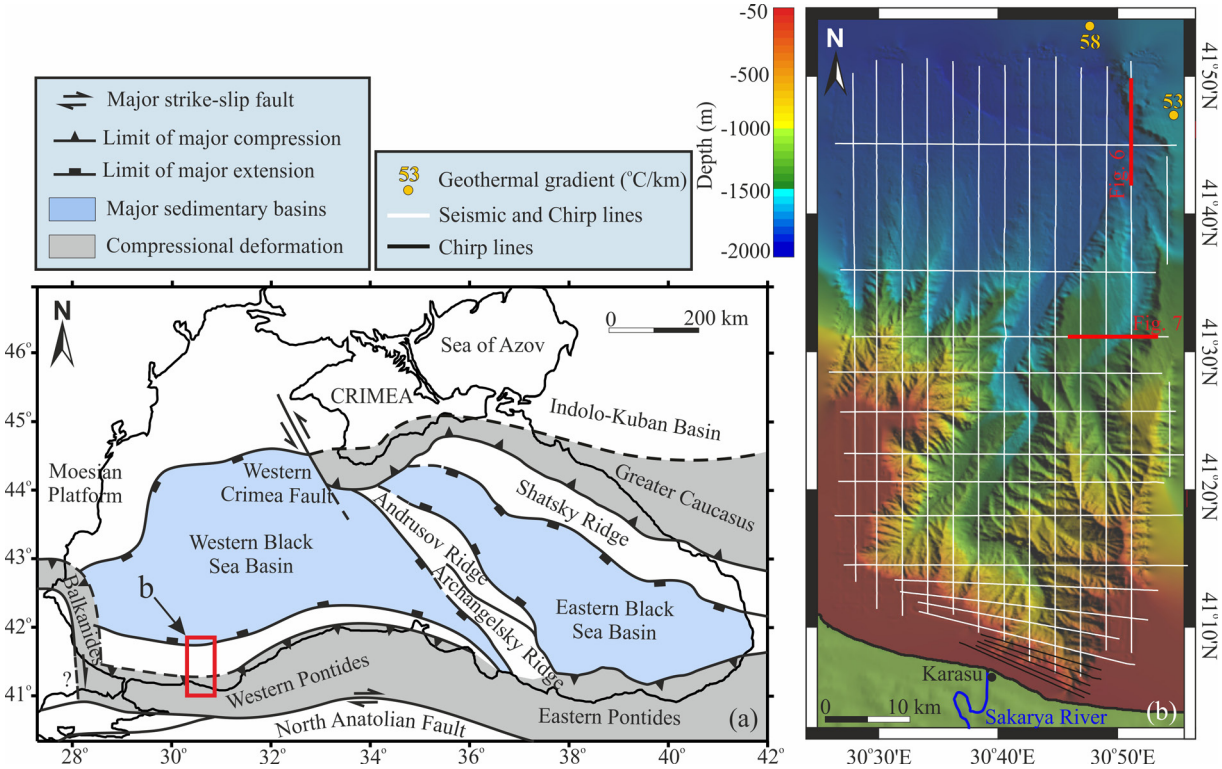

Figure 1. (a) Major tectonic components of the Black Sea and the surrounding region (modified from Finetti et al., 1988; Robinson et al., 1996; Spadini et al., 1996). (b) Locations of the multichannel seismic and 3.5-kHz Chirp subbottom profiler lines on the multibeam bathymetric map of the study area. The geothermal gradient values are from the International Heat Flow Database of the International Heat Flow Commission.

The system utilizes 126 beams providing a total swath coverage of 153° at 1.5° resolution. Processing of the bathymetric data included data loading, beam editing and despiking, correction of navigation errors, data interpolation, digital terrain model (DTM) construction, and gridding at 100-m resolution.

A side-mounted Bathy2010 Chirp subbottom profiler was used to image shallow subsurface sediments. The Chirp system utilizes a sweep signal between 2.75 and 6.75 kHz centered at 3.5 kHz. Processing of the Chirp subbottom profiler data included delay-time correction, dechirping, gain recovery, and amplitude envelope calculations.

4. Data interpretation and analysis

BSRs, gas-charged sediments, and mud volcanoes were mapped using MCS data. Figure 2a shows the distribution of the BSR reflections, acoustically transparent reflection zones commonly associated with shallow gas accumulations, mud volcanoes, and gas chimneys in the study area. BSR reflections are commonly observed in areas where the water depth ranges between 750 and 1950 m and they occupy a total area of approx. 380 km^2. Shallow gas accumulations, on the other hand, are observed in the north and NE of the study area and cover a total area of approx. 200 km^2. Gas chimneys show a random distribution along the continental rise commonly coinciding with a shallow gas zone or a BSR area. The depth of the BSRs from the seafloor increases from south to north being approx. 70 ms to the south and reaching 350 ms at the NW edge of the study area (Figure 2b).

4.1. Characteristics of the BSRs

In seismic profiles, BSRs that mark the base of the gas hydrate accumulations are characterized by high to moderate amplitude reflections with an opposite polarity with respect to the seafloor reflection. From MCS data, BSR reflections are observed especially along the continental rise (Figure 2a). They commonly mimic the seafloor and crosscut the reflections from sedimentary layers where the dipping exists. In most cases, we observe anomalously high-amplitude bright reflections beneath the BSRs (e.g., Figure 3a), which terminate at the BSR level. Typically, acoustically transparent zones exist below these bright reflections. In some cases, gas chimneys through the BSR reflections are also observed (Figures 3a and 3b).

Whenever bright reflections accompany the BSRs, the amplitude of the BSRs are almost four times higher than that of the seafloor reflection. In cases where no bright

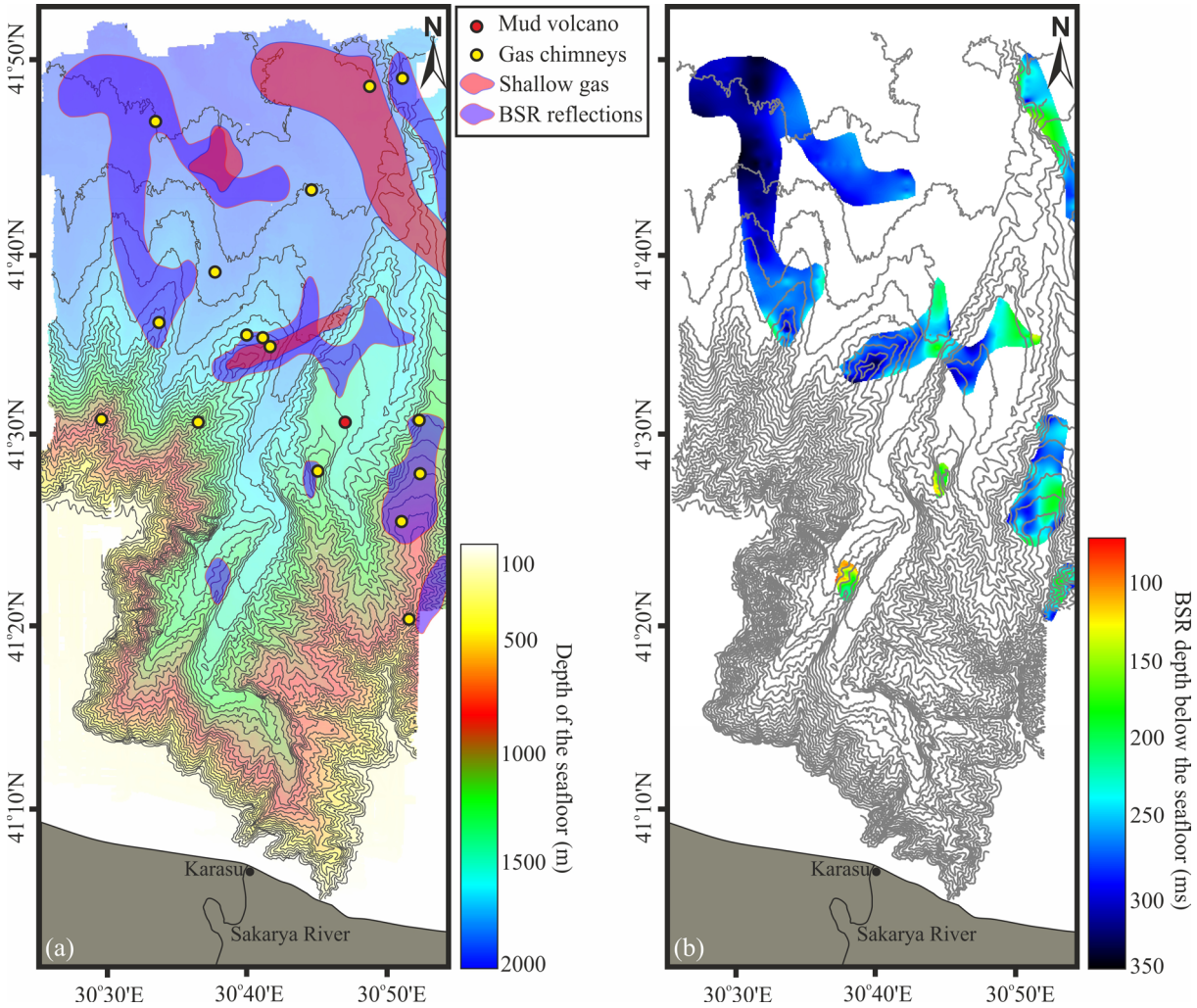

Figure 2. (a) Distributions of the BSRs and the free gas, and the locations of the gas chimneys and the mud volcanoes in the study area. (b) Depths of the BSR reflections below the seafloor in milliseconds deduced from MCS data. Contours correspond to depth.

reflections are associated with the BSRs, the BSRs exhibit amplitudes that are similar to or lower than those of the seafloor reflection. For instance, the amplitude of the BSR reflection in Figure 3c is almost half of the seafloor reflection. Figure 3d shows an NMO-corrected CDP gather indicating the reflection amplitudes down to the BSR depth at approx. 1920 ms. No additional gain except true amplitude recovery to recover the spreading losses has been applied to this data. The BSR has opposite polarity with respect to the seafloor reflection and amplitude of the BSR is approx. 10 times higher than that of the seafloor reflection.

BSRs in the area are identified at the toe of the steep continental slope (Figure 3a), especially below the canyon walls and bases (Figure 3b), as well as beneath the flat plateaus (Figure 3c). To the NW, where a sediment wave field exists, interpreted BSRs appear almost parallel to the sedimentary layers, making them difficult to distinguish especially on seismic lines running in a N-S direction (Figure 3e). BSRs in this area display a shingled appearance and we use seabed-parallel seismic amplitudes, rather than cross-cutting geometries, in order to map them.

4.2. Shallow gas, chimneys, and mud volcanoes

MCS data indicate the presence of acoustically transparent areas in the subsurface that are associated with gas-charged sediments with widths ranging between 1.2 and 6 km (Figures 4a–4e). MCS data show that these zones are located along the continental rise region, especially close to the NE border of the study area (Figure 2a). The gassy sediments mask the deeper reflections due to an excessive attenuation of the seismic signal in these zones producing so-called acoustic turbidity zones (Figure 4a). Because

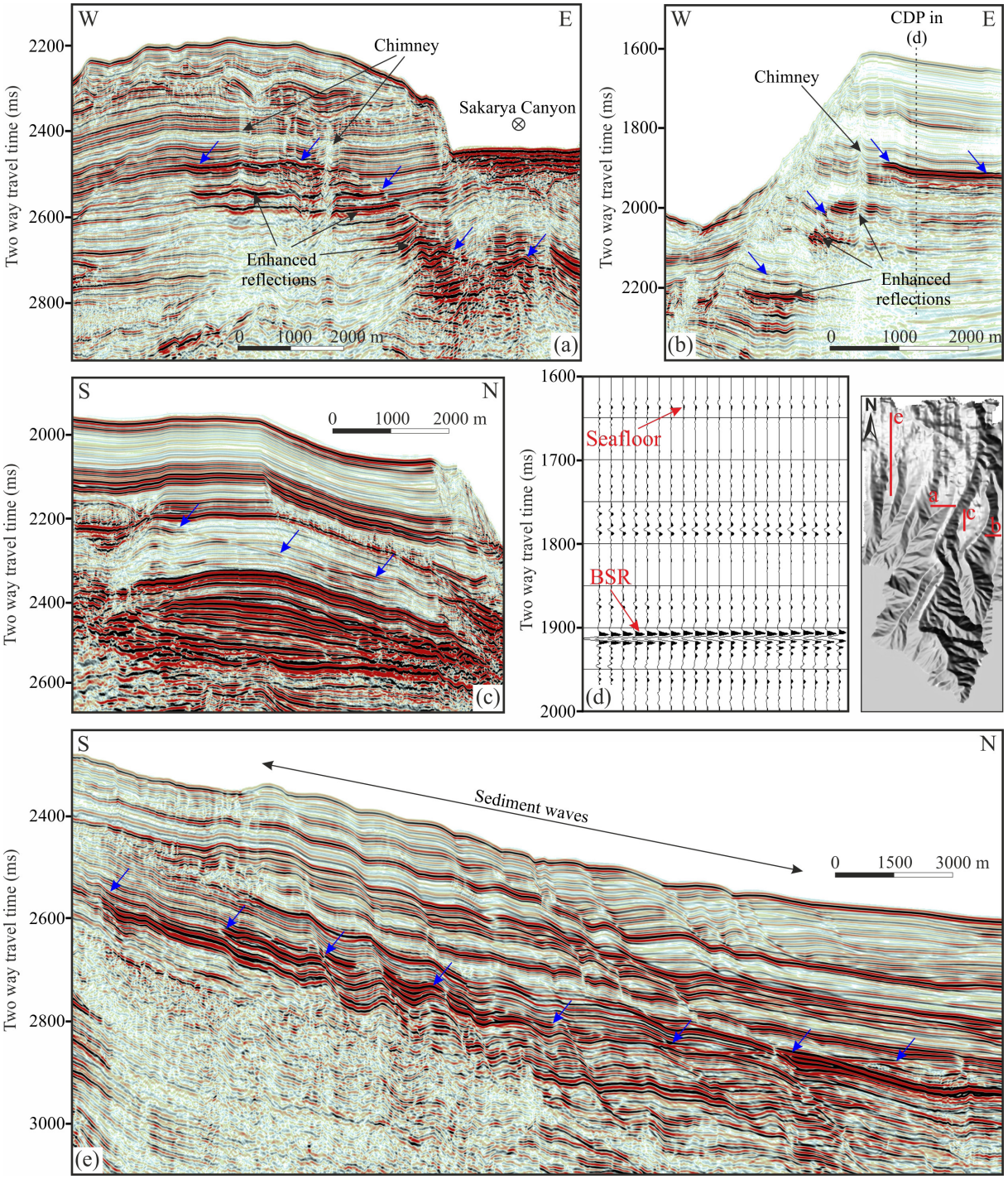

Figure 3. BSR examples on MCS sections from (a) western levee of the Sakarya Canyon, (b) easternmost side of the area, and (c) the flat platform at the NE part of the continental rise. (d) NMO-corrected CDP gather showing the amplitude of the BSR with respect to the seafloor reflection (location of the CDP is shown in (b)). Only spherical divergence correction was applied to the gather in (d). (e) An example MCS line from the NW part of the area showing a BSR reflection subparallel to the stratigraphy. Blue arrows and inset show the BSRs and the locations of the seismic lines on the shaded relief depth map from multibeam bathymetric data, respectively.

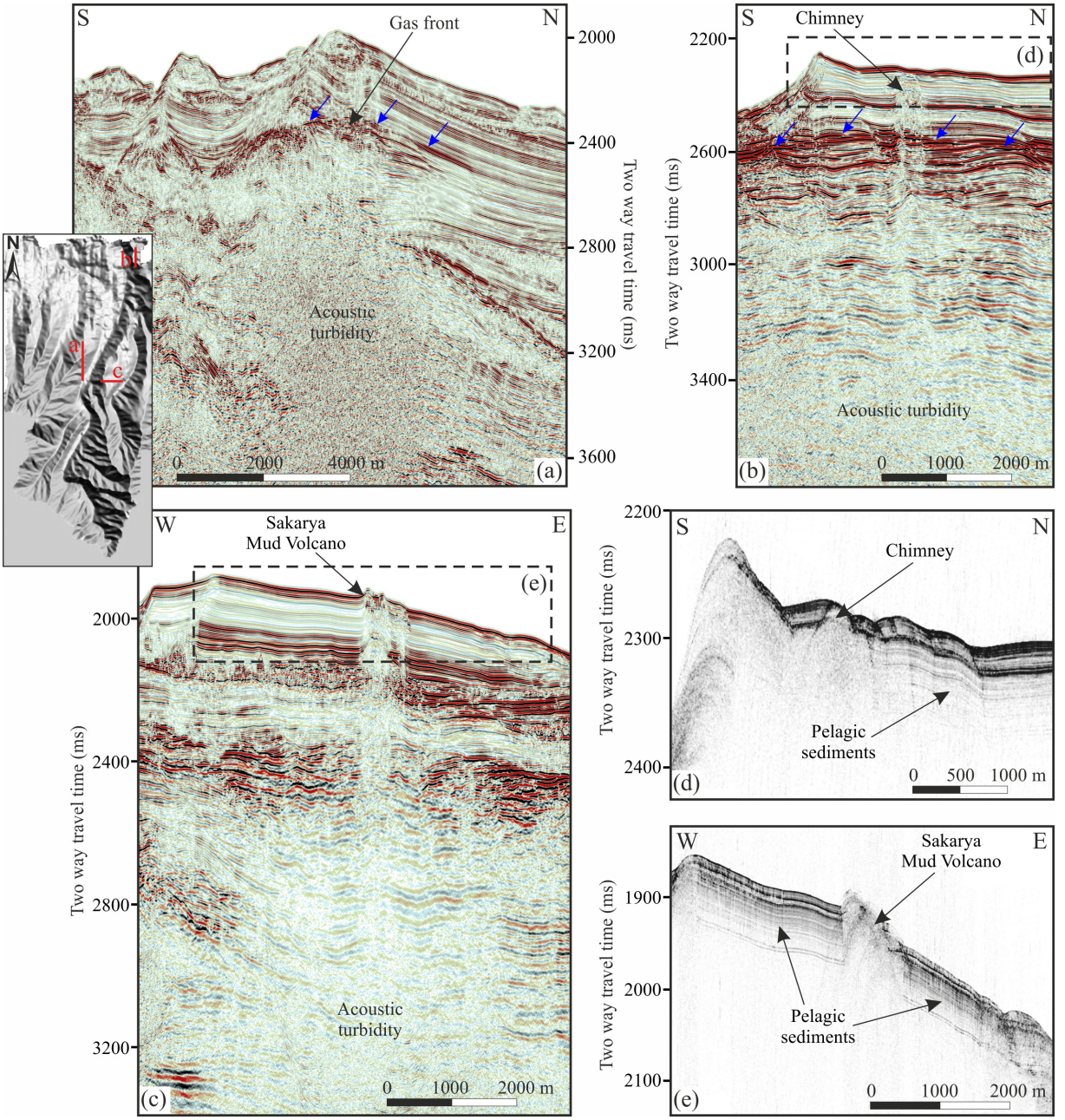

Figure 4. Acoustic turbidity zones and BSR examples on MCS sections from (a) the western levee of the Sakarya Canyon and (b) the flat platform at the NE part of the continental rise. Blue arrows show the BSRs. (c) MCS section showing the newly discovered Sakarya Mud Volcano, (d) Chirp section showing the shallow structure of the gas chimney illustrated in (b), and (e) Chirp section showing the shallow structure of the Sakarya Mud Volcano illustrated in (c). Inset shows the locations of the seismic lines on the shaded relief depth map from multibeam bathymetric data. Dashed rectangles in (b) and (c) show the locations of corresponding Chirp data shown in (d) and (e), respectively.

of the signal attenuation, it is commonly not possible to determine the bottom of the gassy sediments. Although there are sharp vertical boundaries between gas-bearing and gas-free sediments, the top reflection from the acoustic turbidity zone is not a high-amplitude bright reflection, but generally appears blurry in MCS data (Figure 4a). In some cases, the gas front coincides with the BSR, indicating that the BSR acts as a cap rock for the accumulation of shallow gas beneath the gas hydrate layer.

We observe narrow (between 30 and 180 m wide) gas chimneys generally associated with the BSR reflections, rooted in the transparent zones located below the BSRs.

They appear as columnar disturbances or transparent to semitransparent vertical zones in MCS data. The chimney in the seismic line in Figure 4b is approx. 180 m wide and it vertically extends below the BSR level. Unlike the one in the Chirp data shown in Figure 4d, most of the chimneys do not reach the seafloor and do not produce local depressions or pockmarks at the seafloor. In addition, it is typically not possible to determine if these vertical zones are associated with fault surfaces since the attenuation of the acoustic signal produces transparent zones, which almost completely prevent identification of the sedimentary structure.

On the flat platform to the east in the continental rise, MCS data show a newly discovered mud volcano (Figure 4c), which is referred to in this study as the "Sakarya Mud Volcano". It has a relatively narrow (approx. 800 m at the seafloor) feeder channel appearing as an acoustically transparent vertical column. Especially within the shallow sedimentary strata, the layers at both sides of the feeder channel typically bend upwards. It has an asymmetric cone with a positive relief of approx. 15 m at the seafloor (assuming 1500 m/s water velocity). Chirp seismic data in Figure 4e indicate that the topmost structure, possibly containing the material erupted from the volcano, consists of chaotic reflectors, which can be defined as successive reflection hyperbolas of relatively low reflectivity.

4.3. Stability conditions for the gas hydrates

Stability conditions for the gas hydrates mainly depend on the pressure and temperature distribution of the subsurface, known as stability conditions. We observe BSR reflections between 70 and 350 ms below the seafloor (Figure 2b), or between 960 and 2200 m from the sea surface. This indicates that the gas hydrates in the area occur at pressures ranging from approx. 96 to 220 bars. This zone corresponds to the toe of the slope where erosional processes such as gravitational sliding are less observed, higher sedimentation rates exist, and shallow gas within the sediments is widespread. It is also well known that the seafloor temperature in the Black Sea deep basin is quite stable at 9 °C (e.g., Vassilev and Dimitrov, 2002). According to the heat flow measurements conducted within the western Black Sea basin (Kutas et al., 1998; Vassilev and Dimitrov, 2002), the geothermal gradient of the study area is approx. 50 °C/km. Hence, we use this value to calculate the stability conditions of the gas hydrates in the area.

We calculate gas hydrate stability curves with HWHydrate software (Figures 5a–5e) using three different gas compositions in order to test whether heavier hydrocarbon gases exist in the hydrate composition (Figures 5b and 5d): curve I: 100% CH_4; curve II: 90% CH_4, 5% C_2H_6, 3% CO_2, 2% H_2S; curve III: 80% CH_4, 10% C_2H_6, 5% CO_2, 5% H_2S. These compositions are mainly based on the gas chromatography results obtained from the box cores collected offshore of Zonguldak 50 km east of the study area (Küçük, 2016). The seismic lines in Figures 3a and 4b were then converted into the depth domain using average velocities (Figures 5a and 5c) to compare with the calculated stability curves. Estimated depths of the BGHZ for three different geothermal gradient values (40, 50, and 60 °C/km) are also computed and extrapolated along the seismic lines.

The seismic line in Figure 5a contains the closest BSR reflection to the geothermal gradient measurement locations provided by the Global Heat Flow Database (Figure 1). The seafloor in the BSR zone of the seismic line in Figure 5a is of very low gradient, and the BSR mimics the seafloor at a quite stable depth at approx. 190 m below the seabed (that is the thickness of the GHZ at CDP 260). The BSR depth in this seismic line is approximately consistent with the theoretical depth of the BGHZ curve calculated for 50 °C/km. When the BSR depth is projected onto the thermobaric stability curve in Figure 5b, it coincides with the intersection point of the geothermal gradient for 50 °C/km and the stability curve of the gas composition I (pure CH_4 (methane) case) as indicated by IP in Figure 5b.

The seismic line in Figure 5c is from the central part of the study area and contains a BSR reflection along the western levee of the Sakarya Canyon. The seafloor in this seismic line slightly deepens from 1600 to 1800 m towards the east, and the BSR mimics the seafloor at a quite stable depth at approx. 230 m below the seafloor (that is the thickness of the GHZ at CDP 4600). The BSR depth is consistent with the theoretical depth of the BGHZ curve calculated for 50 °C/km to the east, whereas it fits with the curve calculated for 60 °C/km towards the west (Figure 5c). The depth of the BSR coincides with the intersection point of the geothermal gradient for 50 °C/km and the stability curve of the gas composition II (90% CH_4, 5% C_2H_6, 3% CO_2, 2% H_2S case) indicated by IP in Figure 5d.

4.4. Seismic attribute analysis

Since their first introduction in 1970s by Taner et al. (1979), instantaneous attributes (so-called complex trace attributes) have become integral tools in seismic data interpretation as well as reservoir characterization. They are calculated by considering an analytic signal concept using Hilbert transform of the seismic trace. We use the general term "seismic attributes" in this manuscript. A detailed description of the main attributes and their mathematical expressions can be found elsewhere (e.g., Taner et al., 1979; Coren et al., 2001; Kumar et al., 2019). Today, there are several different types of seismic attributes used for different purposes at different stages of seismic interpretation. In this study, we calculate seven seismic attributes to describe and analyze the properties of the reflections received from the base of gas hydrate accumulations (BSR reflections), shallow gas zones, and

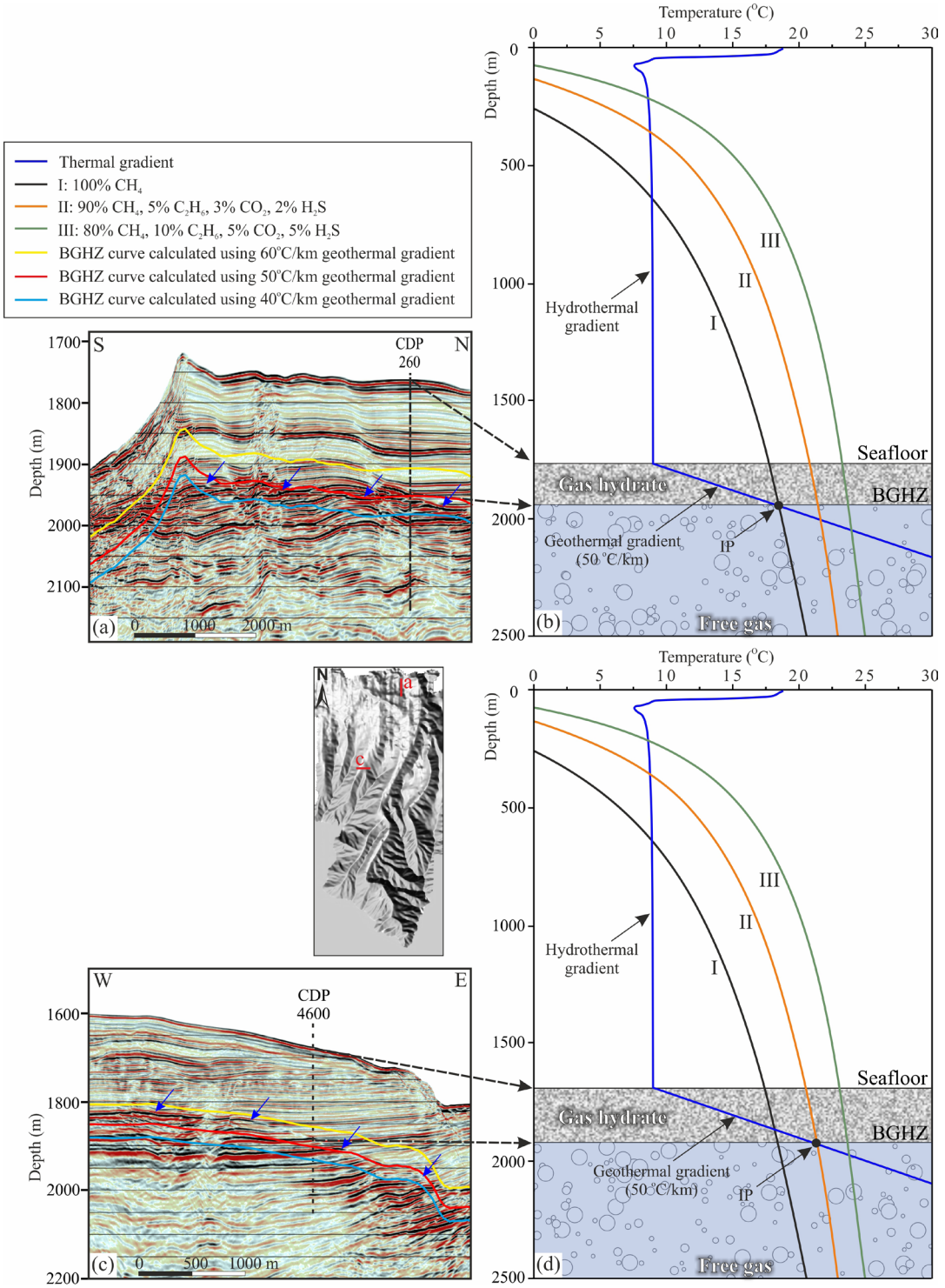

Figure 5. (a) An example seismic line from NE part of the study area with estimated depths of the BGHZ for three different geothermal gradient values (40, 50, and 60 °C/km) superimposed. (b) Gas hydrate stability curves for three different gas compositions and hydrothermal and geothermal gradient curve for 50 °C/km in the location in (a). Geothermal gradient curve for 50 °C/km and stability curve I (pure methane hydrates case) intersect at the BGHZ as indicated by IP. (c) Another example seismic line from central part of the study area with estimated depths of the BGHZ for three different geothermal gradient values (40, 50, and 60 °C/km) superimposed. (d) Gas hydrate stability curves for three different gas compositions and hydrothermal and geothermal gradient curve for 50 °C/km in the location in (c). Geothermal gradient for 50 °C/km and stability curve II (mixed gas hydrates case) intersect at the BGHZ as indicated by IP. Blue arrows show the BSRs. The hydrothermal gradient in (b) and (d) is from a CTD cast performed during the survey. Inset shows the locations of the seismic lines on the shaded relief depth map from multibeam bathymetric data.

mud volcano areas. These attributes can be defined as follows (Taner, 1979):

Amplitude envelope (reflection strength): It is the envelope of the input seismic signal and is always a positive quantity. It is a discriminator for sequence boundaries, bed thickness, spatial correlation of lithologic variations, and strong acoustic impedance contrasts such as those obtained from gas fronts.

Apparent polarity: It is the polarity of amplitude envelope peaks scaled by the envelope value. It describes the polarity of the reflection events, and when compared to the seafloor reflection polarity, it may indicate polarity reversals due to the shallow gas accumulations and BSR reflections.

Instantaneous phase: It is independent of amplitude information and strong and weak events are in the same amplitude level in phase sections. Therefore, it better shows the spatial continuity of the reflections as well as discontinuities like faults or pinch-outs.

Instantaneous frequency: It is the time derivative of instantaneous phase and indicates the time-dependent frequency content of the seismic signal. Hence, it provides information especially about the low-frequency zones below the gas fronts or BSRs due to high attenuation of the seismic signal.

Paraphase: It shows the instantaneous phase with the predictable trend (background component) removed. This attribute is useful for visualizing the stratigraphic details in depositional settings. It can be effectively used to pick reflection events and fault surfaces in areas with low signal quality.

Average energy: It is the section obtained by integrating the envelope section between the events in the paraphase section. It better displays the higher amplitude zones in a seismic section and can therefore be used to track horizons laterally since it highlights stratigraphic details.

Pseudo-relief: These sections are obtained by applying a Hilbert transform to the energy attribute calculated in a time window. It is considered that this attribute removes the effect of seismic wavelets and produces a more consistent seismic image for a better visual analysis of the seismic data, providing an easier interpretation of faults, horizons, and bright spots.

Different seismic attributes are calculated to analyze the reflections from the BSRs and shallow gas accumulations (Figures 6a–6h) as well as the data around the Sakarya Mud Volcano (Figures 7a–7h). The seismic profile in Figure 6a includes an almost horizontal gas front in a scattered form to the south at approx. 2550 ms depth, a BSR reflection lying parallel to the seabed at approx. 250 ms below the seafloor, and a narrow gas chimney associated with this BSR reflection to the north. The reflection strength or amplitude envelope section in Figure 6b displays amplitude anomalies and indicates that the reflection strength of the BSR and gas front is 2.5 times higher with respect to the seafloor reflection amplitude. According to the apparent polarity section in Figure 6c, both the gas front and BSR reflection show opposite polarity: the seafloor reflection is expressed as positive amplitudes shown by red color, while gas front and BSR reflections, on the other hand, are characterized by negative amplitudes expressed by blue color (Figure 6c). The instantaneous phase section in Figure 6d indicates that the lateral continuity of the reflection events is relatively poor below the gas front and along the columnar disruption zone of the chimney. A similar situation in trace-by-trace consistency of the reflections is also observed in the paraphase section shown in Figure 6e. The instantaneous frequency section in Figure 6f indicates that the reflections from the gas front and BSR as well as the sediments around the seafloor are of relatively higher frequency components up to 160 Hz. However, the instantaneous frequency is significantly low at the acoustic turbidity zone below the gas front, beneath the BSR, and along the chimney. These low frequency zones indicate high absorption in the underlying sediments. The average energy section in Figure 6g denotes the reflection energy of the gas front and BSR reflections being as high as the seafloor reflection, while it is relatively lower for the sediments above and below the gas front and the BSR as well as within the chimney. The pseudo-relief section (Figure 6h) clearly shows the event continuity within the section. It illustrates that the gas front and BSR reflection show relatively good reflection continuity, whereas it is quite poor for the reflections especially below the gas front and within the chimney zone.

The seismic profile in Figure 7a includes the Sakarya Mud Volcano to the west and a BSR reflection along a levee to the east. The BSR reflection mimics the seabed at approx. 260 ms below the seafloor, and a narrow gas chimney can be traced down to the acoustic turbidity zone at 2500 ms depth through the BSR reflection. The amplitude envelope section in Figure 7b indicates that the reflection strength of the BSR and gas front is approximately two times higher with respect to the seafloor reflection amplitude. These high amplitude zones, especially the BSR reflection and the shallow layers to the east of the mud volcano, also show polarity reversals in the apparent polarity section in Figure 7c. A relatively small area below the BSR and the entire columnar structure of the Sakarya Mud Volcano show discontinuous reflections in the instantaneous phase and paraphase sections given in Figures 7d and 7e, respectively. The instantaneous frequency section in Figure 7f illustrates a predominant low frequency zone of approx. 60 Hz below 2400 ms. However, especially the reflection from the zone below the BSR from the chimney and the zone within and below the Sakarya Mud Volcano consists

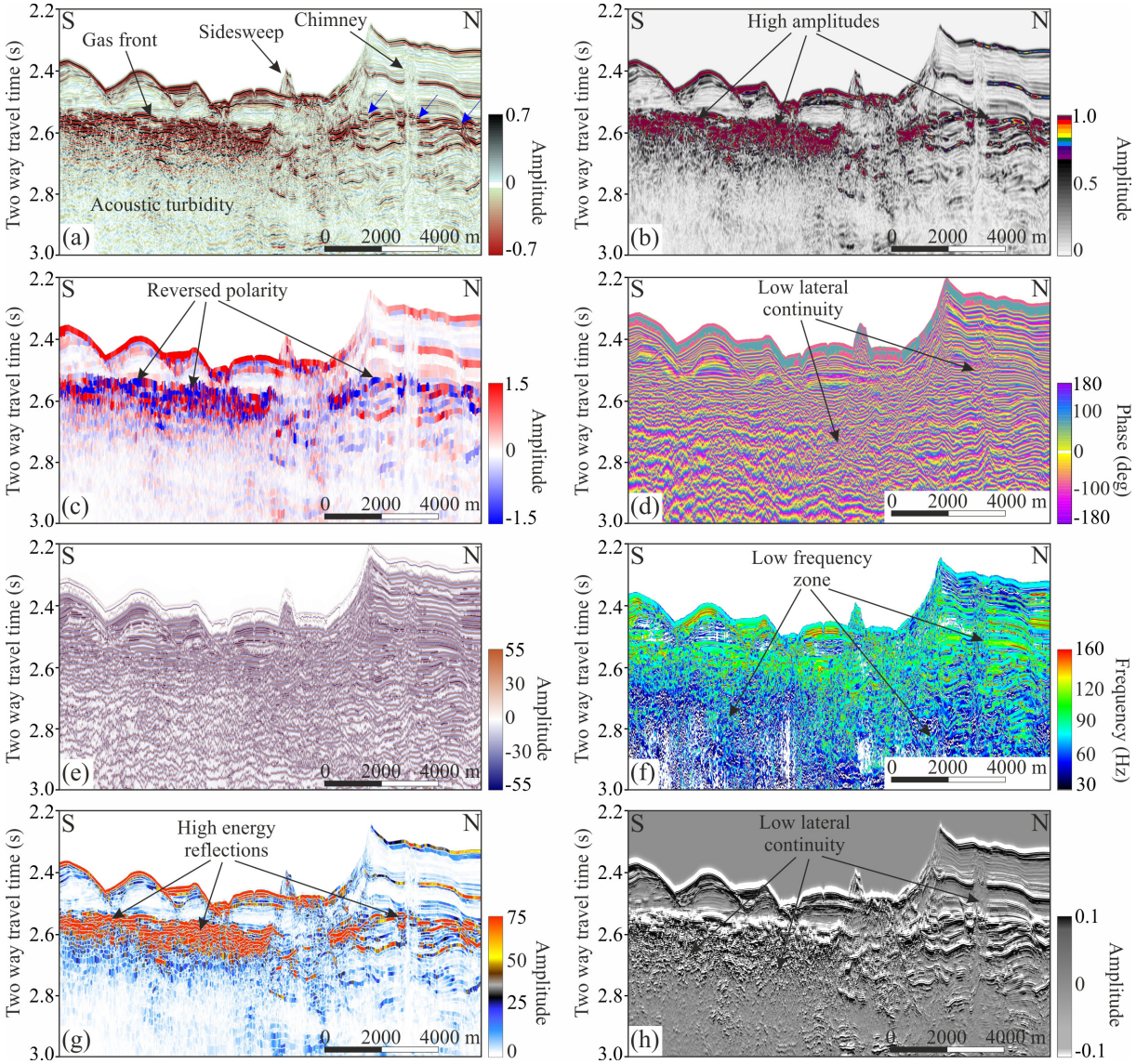

Figure 6. Examples of different seismic attribute sections. (a) True amplitude MCS data, (b) amplitude envelope (reflection strength) section, (c) apparent polarity section, (d) instantaneous phase section, (e) paraphase section, (f) instantaneous frequency section, (g) average energy section, and (h) pseudo-relief section. Blue arrows show the BSR. See Figure 1b for locations of MCS data.

of very low instantaneous frequency values of lower than 30 Hz, indicating high attenuation of the acoustic signal due to the presence of gas in the sediments. According to the average energy section in Figure 7g, BSR reflection and the sediments in the central part of the section show relatively higher reflection energy, whereas the energy is almost zero for the reflections from acoustic turbidity zones below the BSR, from the mud volcano, and within the feeder channel. In the pseudo-relief section (Figure 7h), the amplitude of the BSR reflection and the reflections at both sides of the feeder channel of the Sakarya Mud Volcano are relatively higher with good lateral continuity, whereas the acoustic turbidity zones are characterized by poor trace-by-trace consistency.

5. Discussion

5.1. Properties of the gas hydrates

In the study area, BSR reflections are observed on high-resolution MCS lines between water depths of 750 and 1950 m and at 70 to 350 ms below the seafloor. They show the following general characteristics from the MCS data:

· They are generally high-amplitude reflections. Their amplitudes are at least two times higher than those of seafloor reflections.

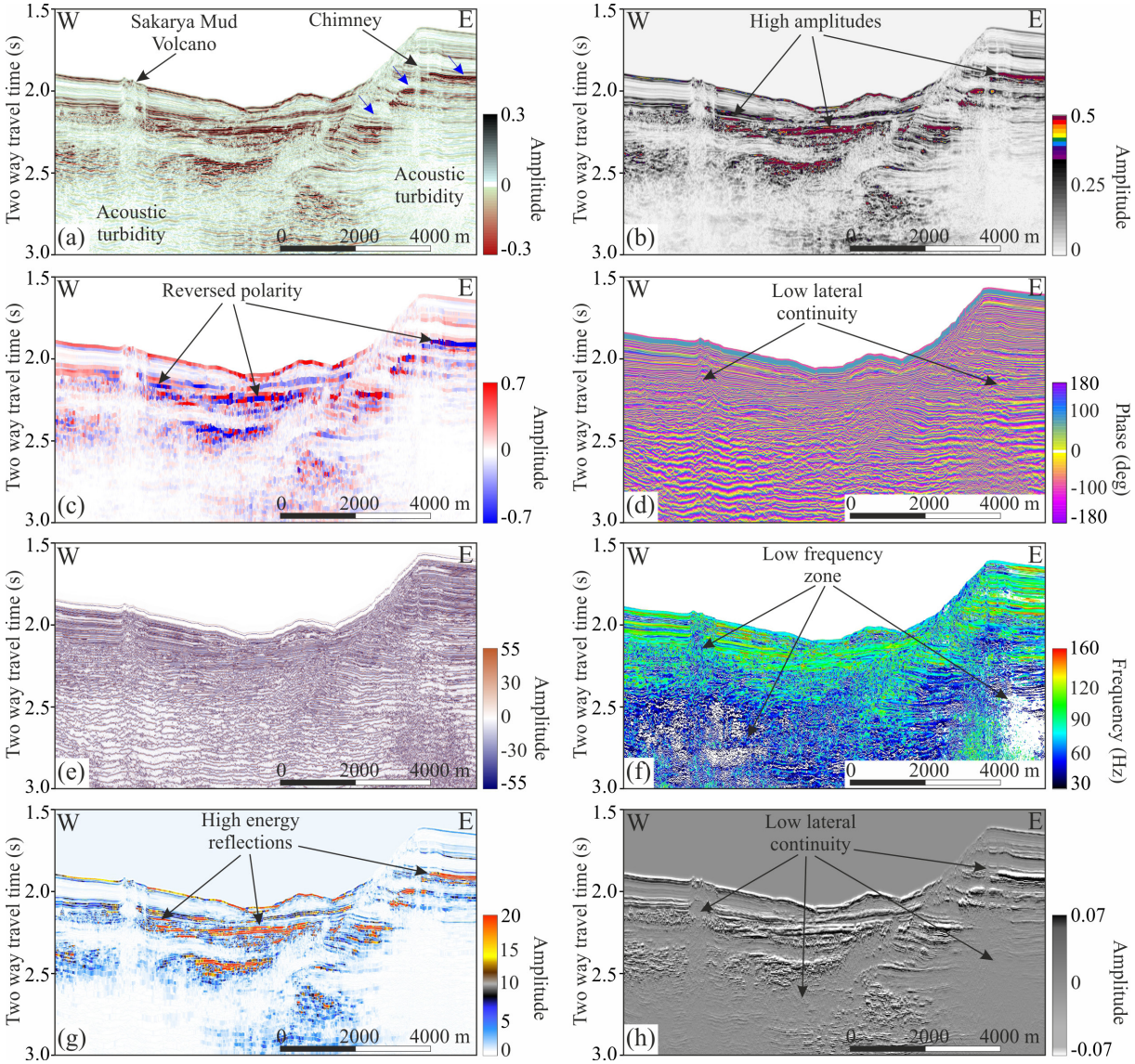

Figure 7. Examples of different seismic attribute sections. (a) True amplitude MCS data, (b) amplitude envelope (reflection strength) section, (c) apparent polarity section, (d) instantaneous phase section, (e) paraphase section, (f) instantaneous frequency section, (g) average energy section, and (h) pseudo-relief section. Blue arrows show the BSR. See Figure 1b for locations of MCS data.

· They are characterized by distinct opposite polarity reflections with respect to the seafloor reflection.

· They generally mimic the seabed and crosscut the reflections that represent the boundaries between the sedimentary layers.

· Acoustic turbidity and/or low frequency reflections are often observed below the BSRs.

· Depth of the BSRs increases with increasing water depth northwards.

Berndt et al. (2004) reported seismic reflections that also crosscut the sedimentary layers. They related this phenomenon to diagenetic boundaries instead of the transition from gas hydrate to gas phase at the BSR level, and they suggested that these types of BSRs were opal-C/opal-AT transition or a smectite/illite conversion, which was also pressure- and temperature-dependent; hence, the reflections from this boundary also mimicked the seabed. However, such reflections do not show opposite polarities with respect to the seafloor and they form at greater depths since they require much higher temperatures (35–50 °C) to form (Berndt et al., 2004; Mosher, 2011). We do not consider that the BSR reflections in our study area are related to the diagenetic boundaries since they show opposite polarity with respect to the seafloor (Figures

6c and 7c) and they occur at relatively shallower depths with 18 to 22 °C subsurface temperatures (Figure 5). Considering their specific characteristics listed above, BSR reflections in the study area are interpreted to be associated with the base of the gas hydrate accumulations (BGHZ) as suggested by several researchers (e.g., Singh et al., 1993; Laberg and Andreassen, 1996; Andreassen et al., 1997; Diaconescu et al., 2001; Lee and Dillon, 2001; Pecher et al., 2001; Bohrmann et al., 2003; Krastel et al., 2003; Talukder et al., 2007; Li et al., 2015).

The thickness of the gas hydrate stability zone depends on various factors, predominantly the gas composition (heavier hydrocarbon gases enlarge the stability zone), geothermal gradient (inversely proportional to the stability zone thickness), water depth and seafloor temperature (directly proportional to the stability zone thickness), and pore-water salinity (stability curve moves to lower temperatures if salinity increases) to a lesser extent (Sloan, 1990; Diaconescu et al., 2001). In the study area, the thickness of the stability zone increases as the water depth increases towards the north, possibly due to the increase of the ambient pressure, making water depth the major controlling factor for the thickness of the gas hydrates.

An acoustic blanking zone above the BGHZ is reported in some cases (Lee et al., 1994; von Huene and Pecher, 1999; Lee and Dillon, 2001; Mosher, 2011), which is caused by the weakening of the reflection amplitudes due to the gas hydrate cementation resulting in homogeneity within the sediments above the BSR (Mosher, 2011). Our MCS data, however, do not show any acoustic blanking zones above the BGHZ (Figures 3, 4, 7, and 8). The amount of blanking indeed depends on the amount of gas hydrate concentrations in the sediments, and Lee and Dillon (2001) proposed that the more gas hydrate concentrations there are in a more porous sedimentary environment, the more significant the amplitude blanking will be above the BGHZ. Therefore, we tentatively suggest that the lack of amplitude blanking above the BSRs in the study area may indicate that the concentrations of the gas hydrates are not considerably high and so they do not establish a homogeneous zone within the GHZ.

Even though the base of the gas hydrate accumulations can be observed from seismic data, it is not possible to identify their top. This phenomenon may be explained in two ways: (i) the gas hydrate concentrations decrease gradually towards the seafloor (Andreassen et al., 1997), or (ii) the limited resolution of seismic data prevents proper imaging (Hyndman and Spence, 1992). We hereby suggest that the upper surface of the gas hydrate accumulations may not be visible from the MCS data since they are in a disseminated form such as relatively small-scale nodules rather than a hydrate-cement model commonly encountered in sandy environments. This is particularly correct for the Black Sea gas hydrates because several researchers reported that they sampled small gas hydrate crystals or finely disseminated gas hydrates dispersed in the mud within the uppermost sediments, especially offshore Crimea and Georgia as well as within the Sorokhin Trough (Limonov et al., 1997; Woodside et al., 1997; Bohrmann et al., 2003; Klaucke et al., 2006; Sahling et al., 2009).

5.2. Free gas beneath the BSRs

Most of the BSR reflections observed worldwide are associated with free gas accumulations below (e.g., Sain et al., 2000; Taylor et al., 2000; Haacke et al., 2007; Mosher, 2011; Yi et al., 2011; Bünz et al., 2012; Faverola et al., 2012; Fohrmann and Pecher, 2012; Wang and Pan, 2017) reaching up to 200–300 m in thickness (Taylor et al., 2000; Grauls, 2001). In the study area, we often observe low-frequency, relatively higher-amplitude reflections terminating against the BSRs (Figures 3a and 3b) or acoustic turbidity zones (Figures 4a and 7), which indicate free gas accumulations under the BSRs. We conclude that the gas hydrates are acting as seals below which the free gas is trapped. Moreover, MCS data also indicate the presence of deep-rooted gas chimneys almost reaching the seafloor through the BSR reflections (Figures 3b, 4b, 6, and 7), which may also be indicative of free gas accumulations below the BSRs. Fault surfaces are generally associated with gas or fluid migration. However, we generally do not observe faults along with the chimneys in the study area (e.g., Figure 3). Therefore, we conclude that the chimneys are formed along the local disruption zones within the shallow sediments, which are possibly enhanced by the upward movement of the fluids. Existence of these local weakness zones through the gas hydrate layer between the seafloor and BGHZ promotes the suggestion that the gas hydrates may be in the form of small-scale nodules within the stability zone. In addition, some of the gas chimneys can pass through the gas hydrate zone above the BGHZ. This may indicate that the fluids forming the chimneys might be warmer than the surrounding strata in the gas hydrate zone resulting in a partial dissociation of the gas hydrates.

On the other hand, there are also gas hydrate accumulations with no free gas indications below the BGHZ, such as those shown in Figure 3c. Pecher et al. (2001) suggested that, in this case, free gas below the BGHZ is consumed by the gas hydrate formation process and transformed into gas hydrates. When there is no gas beneath, the amplitudes of the BSR reflections are relatively weak as compared to the BSR amplitudes with free gas below (Figure 3c). This indicates that the existence of the free gas below the BGHZ dramatically increases the impedance contrast between the gassy and hydrate-bearing sediments resulting in an increased negative reflection coefficient and a much higher-amplitude BSR reflection.

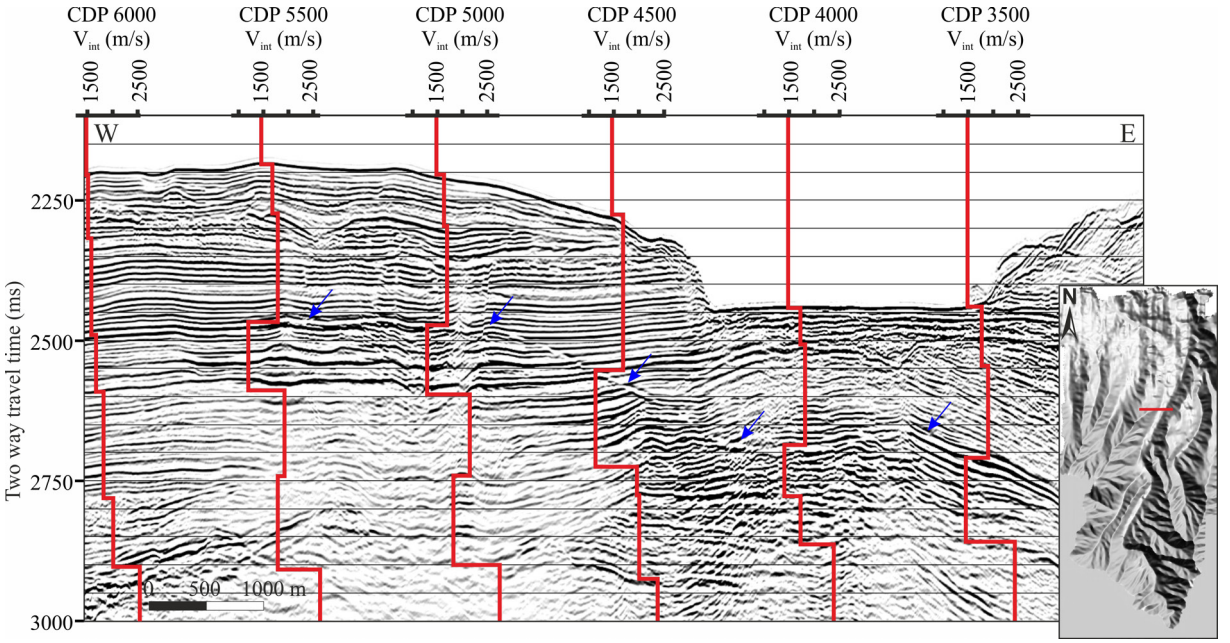

Figure 8. Interval velocity functions (indicated by red curves) along a BSR reflection calculated by Dix equation using RMS velocity picks. Blue arrows show the BSR. Inset shows the location of the seismic line on the shaded relief depth map from multibeam bathymetric data.

Gas hydrate zones have higher impedances than free gas zones, and therefore, we get a negative reflection coefficient at the BGHZ. Figure 8 shows several interval velocity functions along a BSR reflection in the area calculated by the Dix equation using RMS velocity picks from a regular velocity analysis. There is no BSR reflection below the location of CDP 6000, indicating that the velocity of the subsurface increases regularly with increasing depth when no gas hydrates or gas accumulations exist. However, a significant velocity decrease occurs immediately below the BSR reflection, indicated by blue arrows for the rest of the velocity functions in Figure 8, which is attributable to the effect of a free gas accumulation below the BGHZ. Similar velocity anomalies along the BSRs are also reported from several places worldwide, such as from the Ulleung Basin (Horozal et al., 2009), the Oregon ODP site (Andreassen et al., 1997), Canada's Atlantic margin (Mosher, 2011), or the Makran accretionary prism (Sain et al., 2000).

5.3. Seismic attribute analysis

Seismic attributes are often used to analyze and obtain some additional information from BSR reflections by several researchers (e.g., Taylor et al., 2000; Coren et al., 2001; Satyavani et al., 2008; Lee et al., 2017; Kumar et al., 2019). In this study, we calculate seven different seismic attributes to characterize the BSR reflections. The Table summarizes the main results obtained from the seismic attribute analysis.

In gas hydrate studies, seismic attribute analyses provide additional information about the acoustic structure of the BSRs and other structures related to submarine fluid-flow such as mud volcanoes, shallow gas accumulations, and gas chimneys. The reflection strength is controlled by acoustic impedance and hence mainly by the seismic P wave velocity of the subsurface for a constant density medium. Even a small amount of gas in the pore spaces results in a dramatic decrease in the P wave velocity, causing distinct amplitude anomalies on the reflection strength of the seismic data called bright spots (e.g., Taylor et al., 2000; Horozal et al., 2009; Crutchley et al., 2010; Mosher, 2011; Bünz et al., 2012; Rajan et al., 2012). Hence, the high reflectivity, and therefore the high amplitudes on the reflection strength sections, may be explained by various amounts of gas saturations (Taylor et al., 2000). Gas-charged sediments highly absorb the seismic amplitudes, especially those of high-frequency components. Therefore, such low-frequency zones located below the highly reflective zones are commonly attributed to free gas accumulations. The bright spots arising from gas accumulations are also associated with polarity reversals and low-frequency zones lying beneath the bright spots on the apparent polarity and instantaneous frequency sections, respectively.

The attribute analyses shown in Figures 6 and 7 for gassy sediments and BSR reflections indicate that low-frequency zones exist in the instantaneous frequency sections below the high-amplitude reflections on the amplitude envelope sections. These reflections are of opposite polarity with respect to the seafloor reflection, which indicates that

Table. Main results obtained from the seismic attribute analysis.

Attribute	Characterization
Reflection strength	BSR reflections commonly have much higher amplitudes than seafloor reflections, indicating bright or enhanced continuous reflections
Apparent polarity	BSR reflections show polarity reversals with respect to the seafloor reflection
Instantaneous phase	BSRs are somewhat continuous, mimicking the seafloor crosscutting the sedimentary layers
Instantaneous frequency	High-frequency zone is observed above the BSRs; acoustic turbidity zones below the BSRs, along the mud volcano feeder channel and chimneys are characterized by low frequencies
Paraphase	Acoustic turbidity zones, feeder channel, and chimneys appear as discontinuous zones
Average energy	BSR reflections and gas fronts appear as high-energy reflections
Pseudo-relief	BSR reflections are continuous while almost no trace-by-trace consistency exists within the acoustic turbidity zones

a velocity and/or density decrease occurs within the sediments below the highly reflective layers. These zones and chimneys also show amplitude wipeouts and low trace-by-trace consistency in the instantaneous phase and pseudo-relief sections. Therefore, the seismic attribute analysis indicates all of the clues for gas accumulations in the shallow subsurface sediments as well as below the BSR reflections. Gas fronts and BSRs typically appear as high-amplitude continuous reflections in amplitude envelope data (e.g., Taylor et al., 2000; Satyavani et al., 2008). In our study area, however, especially gas fronts are generally characterized by discontinuous high-amplitude reflections, interpreted as suggesting that the upper surface of the gas-charged sediments could be in scattered form. We conclude that this may be due to the lateral variations of the sediment properties within the gas reservoir, i.e. the porosity and/or permeability, and hence the saturation of the free gas varies along the gas front as well as within the gas reservoir.

5.4. BSR irregularities

In some cases, BSRs do not mimic the seafloor. Figure 9 shows an example seismic line with a BSR that deepens over a buried small-scale ridge structure and shallows towards the north. We suggest that there are three possible agents that lead to the formation of BSRs that do not mimic the seabed. These are:

i. Seafloor erosion along the Sakarya Canyon,
ii. Change in the gas composition forming the BSR,
iii. Local change in the geothermal gradient.

5.4.1. Seafloor erosion

Different types of erosional processes that reshape the submarine morphology and transport the sediments from shallow shelf to deep basin can be observed along the continental margins. Paull et al. (2003) showed that submarine slumps or seafloor erosion could release significant quantities of methane directly into the atmosphere because of the decomposition of gas hydrates due to a sudden change in their stability conditions. According to their data from western Africa, Davies et al. (2012) suggested that canyon incision resulted in cooling of the subsurface sediments leading to the deepening of the isothermal boundary. As a result, the BGHZ and hence the BSR also deepened due to this cooling effect of the sediment erosion along the canyons. Davies et al. (2012) also indicated that erosion rates along the canyons are slow enough for cooling and resetting of the BGHZ at the BSR level, which provides enough time for gas hydrates to form within the new BGHZ. Similar observations were also reported from southwest Japan, where even minor seafloor erosion could cause gas hydrate destabilization and methane mobilization and injection into the water column and the atmosphere (Bangs et al., 2010).

The study area hosts Sakarya Canyon, which has individual meandering channels, where different types of erosional processes are observed (Nasıf and Dondurur, 2017; Nasıf et al., 2018). These include gullying, small-scale slumps along the continental rise, gravitational slides along the upper and middle slope, and widespread erosional truncations, especially along the walls and levees of the canyon (Nasıf et al., 2019). Dondurur et al. (2013) indicated that seafloor erosion was also common in offshore Zonguldak, which is located to the eastern part of the study area, and showed interrelations between dissociation of gas hydrates and massive slope failures observed in the continental rise. Truncations are also observed along the canyon floor (Figure 9) where the basal sediments were eroded and redistributed to the deep basin located further to the north.

The sediment truncation on the canyon floor in Figure 9 is evident. This heavy erosion might have resulted in cooling at the BSR level. Deepening of the BGHZ below the canyon floor where the seafloor truncation is maximum

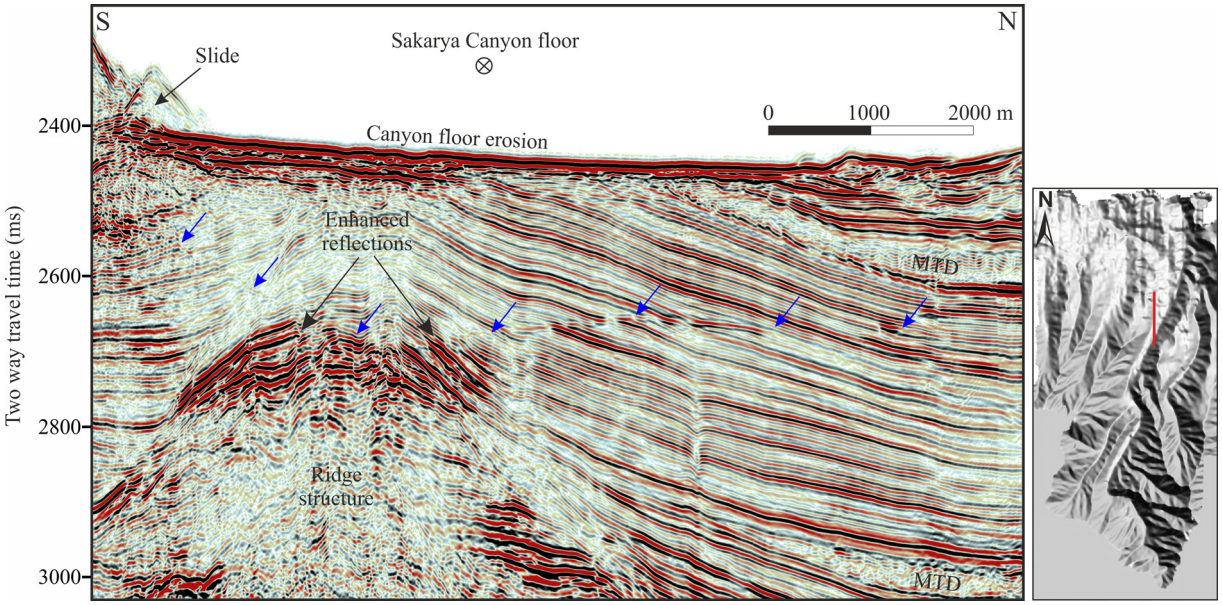

Figure 9. An example seismic line with a BSR (blue arrows) that does not mimic the seafloor. Note that the BSR deepens over a buried small-scale ridge structure and shallows towards the north. MTD stands for mass transport deposits. Inset shows the location of the line on the shaded relief depth map from multibeam bathymetric data.

supports this idea. Bangs et al. (2010) also observed a relict BSR at shallower subsurface depths in their seismic data. They attributed this BSR to BGHZ deepening due to seafloor erosion that occurred for a relatively long period of time. This situation may result in a slow decomposition of preexisting gas hydrate layers originating as a relict BSR as the BGHZ deepens to form a new BSR relatively deeper in the sediments. Our MCS data, however, do not indicate a shallower relict BSR, and we speculate that this may indicate intensive seafloor erosion occurring in a relatively short time span.

The link between erosional processes at the seafloor and stability conditions for gas hydrates is still debated. The formation mechanism for the BSRs that do not mimic the seafloor reflection has been explained by considering seafloor topography with no erosional processes. However, considering that the study area is rather active by means of sediment erosion, it can also be suggested that a stable gas hydrate zone with a BGHZ that mimicked the seafloor existed. Following the seafloor erosion, BGHZ depth changed because of the cooling at the BGHZ level and a new BSR formed at relatively deeper parts in the sediments.

5.4.2. Change in gas composition

Another possible factor that results in a BSR that does not mimic the seafloor could be the change of gas composition forming the gas hydrates along the BSR. We do not have sediment cores recovered from the BSR zones or gassy sediments in the area, and therefore, we do not know the exact gas composition within the sediments and gas hydrates. However, previous studies indicated that both biogenic and thermogenic gases coexist in the study area. Küçük (2016) collected several box cores from the continental rise in offshore Zonguldak, 50 km east of the study area. The average total organic carbon (TOC) of the samples was 2% and gas chromatography results indicated that the gas in the sediments was predominantly methane and propane (in some minor cases, ethane) with minor n-butane. In addition, Turkish Petroleum has been producing dry gas of mixed origin from Eocene turbidites in the Akçakoca Field (Menlikli et al., 2009) located approx. 25 km east of the study area. This situation indicates that the area may be productive by means of thermogenic gas, and there are deep-rooted fault systems (Finetti et al., 1988; Yiğitbaş et al., 2004) that can act as the conduits for deep thermogenic gases for vertical transportation into the shallow sediments where the gas hydrates are stable.

Different gas compositions require different thermobaric conditions to remain in the hydrate phase, i.e. pure methane hydrates require lower temperatures for a constant pressure or higher pressures for a constant temperature than mixed gas hydrates, which contain heavier hydrocarbon gases (Figure 5b). Therefore, if the gas composition changes laterally within the gas hydrate zone above the BGHZ, the depth of the BSR may also change according to the required thermobaric conditions. For instance, if there is a gradual change from a pure methane hydrate to a mixed hydrate in the lateral direction, then the BSR gets deeper since mixed hydrates can be stable at higher temperatures and lower pressures than pure methane hydrates. This phenomenon should be mainly

controlled by subsurface temperature rather than pressure since the BSRs are observed at water depths of between 750 and 1950 m in the study area, which already provides high pressures for the gas hydrates to be stable.

This situation is also evident in the analysis given in Figure 5, which shows stability curves for two different zones in the area for different gas compositions. Stability conditions for the gas hydrates from the NE of the study area (Figure 5a) correspond to a stability curve for pure methane hydrates (IP in Figure 5b). The stability conditions for the central part of the area (Figure 5c), however, coincide with the stability curve for a mixed gas hydrate (IP in Figure 5d). This may indicate that the gas hydrates in different places in this area might be formed by different gas compositions depending on the local conditions where they occur.

5.4.3. Change in geothermal gradient

Another factor that results in an irregular BSR formation is local changes in the heat flow and hence in the geothermal gradient. The heat flow may be affected by several factors, such as sediment lithology, existence of cold/hot fluids within the subsurface, or local undulations of the basement (e.g., Ganguly et al., 2000; Lüdmann et al., 2004; Satyavani et al., 2008; Pecher et al., 2010; Shedd et al., 2012). However, regional MCS data do not indicate regional undulations, such as ridge structures along the continental rise of the study area. Although we observe much smaller and local ridge structures in the shallow subsurface, such as the one shown in Figure 9, their connection to much deeper and regional structures is not known. Therefore, this situation should be verified with local heat flow measurements along a BSR reflection.

5.5. A conceptual model

Following the analysis of available acoustic data, we hereby suggest a model quite similar to those observed in the other margins of the world's oceans for gas hydrate formation in the area (Figure 10). Considering the gas hydrates containing mixed gas of both thermogenic and biogenic origin, we propose that thermogenic fluids from deeper gas sources migrated into the GHZ at shallower sediments. When the gas hydrates formed in the GHZ, their base (BSR) acted as a cap rock for the subsequently migrating gas, and the gas moved in the porous sediments laterally (Figure 10). Whenever these free gas-bearing porous (possibly sandy) layers were crosscut by the BGHZ due to irregularities on the seafloor (such as levees) that led to a sudden downward shift in the BSR, the free gas accumulated below the BSR and formed acoustic anomalies of high-amplitude and low-frequency reflections in the MCS data. However, we still do not know the characteristics and lithology of the sediments in both hydrate and gas-bearing zones. Therefore, the model should be tested by ground truth data by means of both rock properties such as lithology and porosity, and gas types in both gas hydrates and free gas below the BSR.

6. Conclusions

In the western Black Sea margin, high-resolution MCS lines show BSR reflections in the continental rise area at water depths between 750 and 1950 m, lying between 70 to 350 ms below the seafloor, and they are interpreted as the base of the gas hydrate stability zone. They show the general characteristics of BSR reflections, such as high amplitudes, opposite polarity with respect to the seafloor, mimicking of the seafloor, and acoustic turbidity within the underlying

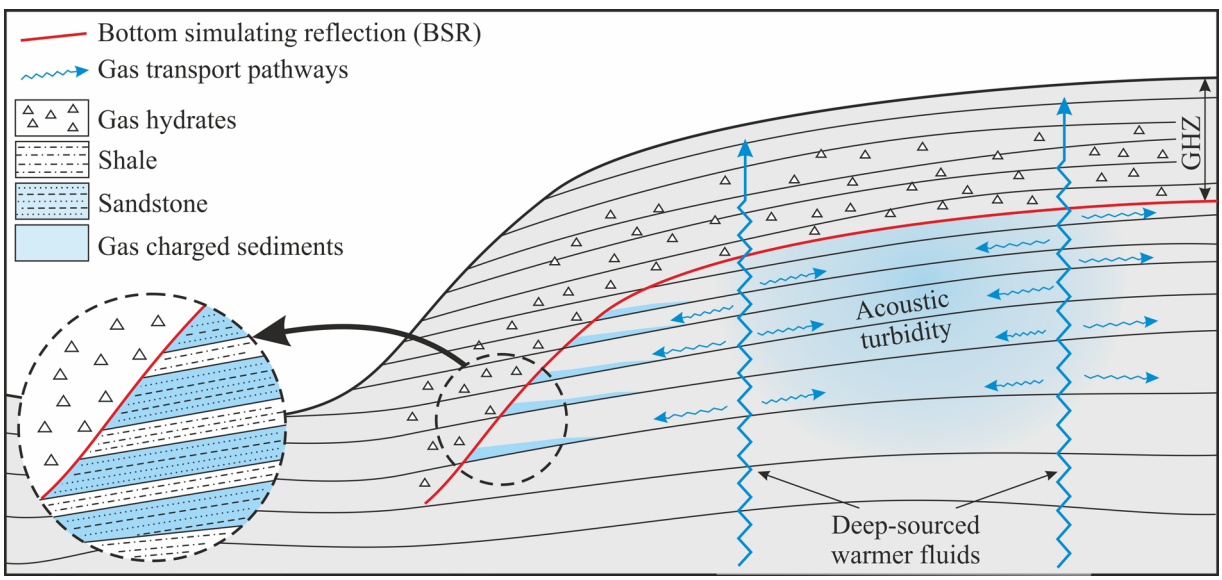

Figure 10. A conceptual model for the gas hydrate formation in the area. See text for details.

sediments indicating free gas accumulations. Seismic attribute analyses reveal that the BSRs and acoustic turbidity zones show the typical characteristics of gas hydrate accumulations with free gas zones under the BSRs. We therefore conclude that free gas accumulations exist beneath most of the BSRs in the area.

Due to the lack of ground truth data, we do not know the exact composition of the gas forming the gas hydrates. However, existence of hydrocarbon production wells nearby, the analysis of shallow sediment samples close to the study area, and thermobaric stability analysis of the gas hydrates indicate that a thermogenic gas component might exist in the gas hydrate composition forming the mixture gas hydrates.

In some cases, BSRs in the area do not mimic the seafloor. We conclude that the reasons for this are (i) seabed erosion along the Sakarya Canyon, (ii) change in the gas composition forming the BSR, and (iii) local changes in the geothermal gradient. We hereby suggest that, depending on the stability conditions for the gas hydrates in the study area, the depths of the BSRs may vary according to the required local thermobaric conditions if the gas composition changes laterally within the GHZ.

Gas chromatography analysis of the sediment samples recovered from BSR zones will provide additional information on the gas composition forming the gas hydrates in the area. Local measurements of the heat flow and/or geothermal gradient will provide subsurface temperature distribution, and both types of data will ensure a more correct stability analysis for the gas hydrates. This information, along with porosity calculations for the sediments within the GHZ, may allow us to compute the total volume of gas hydrates as well as the total methane involved in the gas hydrates in the area.

Acknowledgments

We would like to thank the officers and crew of the *R/V K. Piri Reis* research vessel for their valuable efforts during the data acquisition. The MCS data were processed by SeisSpace Promax software from Landmark Graphics and analyzed using IHS Kingdom Suite Software. This work was supported by a grant from the Scientific and Technological Research Council of Turkey (TÜBİTAK, project code 108Y110). The three anonymous reviewers are thanked for their constructive comments. This work is a part of PhD thesis of Aslıhan Nasıf.

References

Amouroux D, Roberts G, Rapsomanikis S, Andreae MO (2002). Biogenic gas (CH4, N2O, DMS) emission to the atmosphere from near-shore and shelf waters of the north-western Black Sea. Estuarine, Coastal and Shelf Science 54 (3): 575-587.

Andreassen K, Hart PE, MacKay M (1997). Amplitude versus offset modeling of the bottom simulating reflection associated with submarine gas hydrates. Marine Geology 137 (1-2): 25-40.

Bangs NL, Hornbach MJ, Moore GF, Park JO (2010). Massive methane release triggered by seafloor erosion offshore southwest Japan. Geology 38 (11): 1019-1022.

Berndt C, Bünz S, Clayton T, Mienert J, Saunders M (2004). Seismic character of bottom simulating reflectors; examples from the mid-Norwegian margin. Marine and Petroleum Geology 21 (6): 723-733.

Bohrmann G, Ivanov M, Foucher JP, Spiess V, Bialas J et al. (2003). Mud volcanoes and gas hydrates in the Black Sea: new data from Dvurechenskii and Odessa mud volcanoes. Geo-Marine Letters 23 (3-4): 239-249.

Bünz S, Polyanov S, Vadakkepuliyambatta S, Consolaro C, Mienert J (2012). Active gas venting through hydrate–bearing sediments on the Vestnesa Ridge, offshore W-Svalbard. Marine Geology 332-334: 189-197.

Coren F, Volpi V, Tinivella U (2001). Gas hydrate physical properties imaging by multi-attribute analysis–Blake Ridge BSR case history. Marine Geology 78 (1-4): 197-210.

Crutchley GJ, Pecher IA, Gorman AR, Henrys SA, Greinert J (2010). Seismic imaging of gas conduits beneath seafloor seep sites in a shallow marine gas hydrate province, Hikurangi Margin, New Zealand. Marine Geology 272 (1-4): 114-126.

Davies RJ, Thatcher KE, Mathias SA, Yang J (2012). Deepwater canyons: An escape route for methane sealed by methane hydrate. Earth and Planetary Science Letters 323-324: 72-78.

Diaconescu CC, Kieckhefer RM, Knapp JH (2001). Geophysical evidence for gas hydrates in the deep water of the South Caspian Basin, Azerbaijan. Marine and Petroleum Geology 18 (2): 209-221.

Dimitrov LI (2002). Contribution to atmospheric methane by natural seepages on the Bulgarian continental shelf. Continental Shelf Research 22 (16): 2429-2442.

Dondurur D, Çifçi G (2007). Acoustic Structure and recent sediment transport processes on the continental slope of Yeşilırmak River fan, Eastern Black Sea. Marine Geology 237 (1-2): 37-53.

Dondurur D, Küçük HM, Çifçi G (2013). Quaternary mass wasting on the western Black Sea margin, offshore of Amasra. Global and Planetary Change 103: 248-260.

Ergün M, Dondurur D, Çifçi G (2002). Acoustic evidence for shallow gas accumulations in the sediments of the Eastern Black Sea. Terra Nova 14 (5): 313-320.

Faverola A, Bünz S, Mienert J (2012). The free gas zone beneath gas hydrate bearing sediments and its link to fluid flow: 3-D seismic imaging offshore mid-Norway. Marine Geology 291-294: 211-226.

Finetti I, Bricchi G, Del Ben A, Pipan M, Xuan Z (1988). Geophysical study of the Black Sea. Bolletino Di Geofisica Teorika Ed Applicata 30: 197-324.

Fohrmann M, Pecher IA (2012). Analysing sand-dominated channel systems for potential gas-hydrate-reservoirs using an AVO seismic inversion technique on the Southern Hikurangi Margin, New Zealand. Marine and Petroleum Geology 38 (1): 19-34.

Ganguly N, Spence GD, Chapman NR, Hyndman RD (2000). Heat flow variations from bottom simulating reflectors on the Cascadia margin. Marine Geology 164 (1-2): 433-460.

Ginsburg GD, Soloviev VA (1997). Methane migration within the submarine gas–hydrate stability zone under deep-water conditions. Marine Geology 137 (1-2): 49-57.

Grauls D (2001). Gas hydrates: importance and applications in petroleum exploration. Marine and Petroleum Geology 18: 519-523.

Haacke RR, Westbrook GK, Hyndman RD (2007). Gas hydrate, fluid flow and free gas: formation of the bottom-simulating reflector. Earth and Planetary Science Letters 261 (3-4): 407-420.

Hillman JIT, Burwicz E, Zander T, Bialas J, Klaucke I et al. (2018). Investigating a gas hydrate system in apparent disequilibrium in the Danube Fan, Black Sea. Earth and Planetary Science Letters 502: 1-11.

Horozal Ş, Lee GH, Yi BY, Yoo DG, Park KP et al. (2009). Seismic indicators of gas hydrate and associated gas in the Ulleung Basin, East Sea (Japan Sea) and implications of heat flows derived from depths of the bottom-simulating reflector. Marine Geology 258 (1-4): 126-138.

Hyndman RD, Spence GD (1992). A seismic study of methane hydrate marine bottom simulating reflectors. Journal of Geophysical Research 97 (B5): 6683-6698.

Ivanov MK, Limonov AF, van Weering TCE (1996). Comparative characteristics of the Black Sea and Mediterranean Ridge mud volcanoes. Marine Geology 132 (1-4): 253-271.

Ivanov MK, Woodside JM (1996). Shallow gas and gas hydrates on the Crimean continental margin, Black Sea. In: Abstract on Gas Hydrates: Relevance to World Margin Stability and Climatic Change, Ghent, Belgium, p. 46.

Klaucke I, Sahling H, Weinrebe W, Blinova V, Bürk D et al. (2006). Acoustic investigation of cold seeps offshore Georgia, eastern Black Sea. Marine Geology 231 (1-4): 51-67.

Klauda JB, Sandler SI (2003). Predictions of gas hydrate phase equilibria and amounts in natural sediment porous media. Marine and Petroleum Geology 20 (5): 459-470.

Körber JH, Sahling H, Pape T, dos Santos Ferreira C, MacDonald I et al. (2014). Natural oil seepage at Kobuleti Ridge, eastern Black Sea. Marine and Petroleum Geology 50: 68-82.

Korsakov OD, Byakov YA, Stupak SN (1989). Gas hydrates in the Black Sea Basin. Sovetskaya Geologiya 12: 3-10.

Krastel S, Spiess V, Ivanov M, Weinrebe W, Bohrmann G et al. (2003). Acoustic investigations of mud volcanoes in the Sorokin Trough, Black Sea. Geo-Marine Letters 23 (3-4): 230-238.

Küçük HM (2016). Batı Karadeniz Zonguldak–Amasra açıklarında gaz ve gaz hidratların jeolojik ve jeofizik yöntemlerle araştırılması. PhD, Dokuz Eylül University, İzmir, Turkey (in Turkish).

Kumar J, Sain K, Arun KP (2019). Seismic attributes for characterizing gas hydrates: a study from the Mahanadi offshore, India. Marine Geophysical Research 40 (1): 73-86.

Kutas RI, Kobolev VP, Tsvyashchenko VA (1998). Heat flow and geothermal model of the Black Sea depression. Tectonophysics 291 (1-4): 91-100.

Kvenvolden KA, Ginsburgh GD, Soloviev VA (1993). Worldwide distribution of subaquatic gas hydrates: Geo-Marine Letters 13 (1): 32-40.

Laberg JS, Andreassen K (1996). Gas hydrate and free gas indications within the Cenozoic succession of the Bjørnøya Basin, western Barents Sea. Marine and Petroleum Geology 13 (8): 921-940.

Lee J, Byun J, Kim B, Yoo DG (2017). Delineation of gas hydrate reservoirs in the Ulleung Basin using unsupervised multi-attribute clustering without well log data. Journal of Natural Gas Science and Engineering 46: 326-337.

Lee MW, Dillon WP (2001). Amplitude blanking related to the pore-filling of gas hydrate in sediments. Marine Geophysical Researches 22 (2): 101-109.

Lee MW, Hutchinson DR, Agena WF, Dillon WP, Miller JJ et al. (1994). Seismic character of gas hydrates on the southeastern U.S. continental margin. Marine Geophysical Researches 16 (3):163-184.

Lericolais G, Bulois C, Gillet H, Guichard F (2009). High frequency sea level fluctuations recorded in the Black Sea since the LGM. Global and Planetary Change 66 (1-2): 65-75.

Li L, Liu H, Zhang X, Lei X, Sha Z (2015). BSRs, estimated heat flow, hydrate-related gas volume and their implications for methane seepage and gas hydrate in the Dongsha region, northern South China Sea. Marine and Petroleum Geology 67: 785-794.

Limonov AF, van Weering TJCE, Kenyon NH, Ivanov MK, Meisner LB (1997). Seabed morphology and gas venting in the Black Sea mudvolcano area: observations with the MAK-1 deep-tow sidescan sonar and bottom profiler. Marine Geology 137 (1-2): 121-136.

Lüdmann T, Wong HK, Konerding P, Zillmer M, Petersen J et al. (2004). Heat flow and quantity of methane deduced from a gas hydrate field in the vicinity of the Dnieper Canyon, northwestern Black Sea. Geo-Marine Letters 24 (3): 182-193.

Menlikli C, Demirer A, Sipahioğlu Ö, Körpe L, Aydemir V (2009). Exploration plays in the Turkish Black Sea. The Leading Edge 28 (9): 1066-1075.

Merey Ş, Sinayuç Ç (2016). Investigation of gas hydrate potential of the Black Sea and modelling of gas production from a hypothetical Class 1 methane hydrate reservoir in the Black Sea conditions. Journal of Natural Gas Science and Engineering 29: 66-79.

Milkov AV, Sassen R (2002). Economic geology of offshore gas hydrate accumulations and provinces. Marine and Petroleum Geology 19 (1): 1-11.

Minshull TA, Keddie A (2010). Measuring the geotherm with gas hydrate bottom-simulating reflectors: a novel approach using three-dimensional seismic data from the eastern Black Sea. Terra Nova 22 (2) 131-136.

Mosher DC (2011). A margin-wide BSR gas hydrate assessment: Canada's Atlantic margin. Marine and Petroleum Geology 28 (8): 1540-1553.

Murray J, Stewart K, Kassakian S, Krynytzky M, DiJulio D (2007). Oxic, suboxic, and anoxic conditions in the Black Sea. In: Yanko-Hombach V, Gilbert A, Panin N, Dolukhanov P (editors). The Black Sea Flood Question: Changes in Coastline, Climate, and Human Settlement. Berlin, Germany: Springer, pp. 1-21.

Nasıf A, Dondurur D (2017). The morpho-acoustic structure of Sakarya Canyon, southwestern Black Sea. In: European Geosciences Union General Assembly, Vienna, Austria.

Nasıf A, Özel FE, Dondurur D (2018). Morpho-acoustic structure of Sakarya Canyon. In: 3rd National Marine Sciences Symposium, İzmir, Turkey, pp. 318-319 (in Turkish).

Nasıf A, Özel FE, Dondurur D (2019). Morphology and recent sediment distribution along the Sakarya Canyon: preliminary results from seismic data. In: 72nd Turkish Geological Congress, Ankara, Turkey, pp. 907-911 (in Turkish).

Naudts L, Batist M, Greinert J, Artemov Y (2009). Geo- and hydro-acoustic manifestations of shallow gas and gas seeps in the Dnieper paleodelta, northwestern Black Sea. The Leading Edge 28 (9): 1030-1040.

Nomokonov VP, Stupak SN (1988). Indications of gas hydrate deposits in the Black Sea. Geologiya i Razvedka 3: 72-82.

Okay AI, Şengör AMC, Görür N (1994). Kinematic history of the opening of the Black Sea and its effect on the surrounding regions. Geology 22 (3): 267-270.

Okyar M, Ediger V (1999). Seismic evidence of shallow gas in the sediment on the shelf off Trabzon, southeastern Black Sea. Continental Shelf Research 19 (5): 575-587.

Pape T, Bahr A, Klapp SA, Abegg F, Bohrmann G (2011). High-intensity gas seepage causes rafting of shallow gas hydrates in the southeastern Black Sea. Earth and Planetary Science Letters 307: 35-46.

Parlaktuna M, Erdoğmuş T (2001). Natural gas hydrate potential of the Black Sea. Energy Sources 23: 203-211.

Panin N, Popescu I (2007). The northwestern Black Sea: climatic and sea-level changes in the Late Quaternary. In: Yanko-Hombach V, Gilbert A, Panin N, Dolukhanov P (editors). The Black Sea Flood Question: Changes in Coastline, Climate, and Human Settlement. Berlin, Germany: Springer, pp. 387-404.

Paull CK, Brewer PG, Ussler W, Peltzer ET, Rehder G et al. (2003). An experiment demonstrating that marine slumping is a mechanism to transfer methane from seafloor gas-hydrate deposits into the upper ocean and atmosphere. Geo-Marine Letters 22 (4): 198-203.

Pecher IA., Henrys SA, Wood WT, Kukowski N, Crutchley GJ, et al. (2010). Focussed fluid flow on the Hikurangi Margin, New Zealand – Evidence from possible local upwarping of the base of gas hydrate stability. Marine Geology 272 (1): 99-113.

Pecher IA, Kukowski N, Huebscher C, Greinert J, Bialas J et al. (2001). The link between bottom simulating reflections and methane flux into the gas hydrate stability zone new evidence from Lima Basin, Peru Margin. Earth and Planetary Science Letters 185 (3-4): 343-354.

Popescu I, Batist M, Lericolais G, Nouzé H, Poort J et al. (2006). Multiple bottom-simulating reflections in the Black Sea: potential proxies of past climate conditions. Marine Geology 227 (3-4): 163-176.

Rajan A, Mienert J, Bünz S (2012). Acoustic evidence for a gas migration and release system in Arctic glaciated continental margins offshore NW-Svalbard. Marine and Petroleum Geology 32 (1): 36-49.

Robinson A, Spadini G, Cloetingh S, Rudat J (1995). Stratigraphic evolution of the Black Sea: inferences from basin modeling. Marine and Petroleum Geology 12 (8): 821-835.

Robinson AG, Rudat JH, Banks CJ, Wiles RLF (1996). Petroleum geology of the Black Sea. Marine and Petroleum Geology 13 (2): 195-223.

Römer M, Sahling H, Pape T, Bahr A, Feseker T et al. (2012). Geological control and magnitude of methane ebullition from a high-flux seep area in the Black Sea—the Kerch seep area. Marine Geology 319-322: 57-74.

Ryan WB, Pitman WC, Major CO, Shimkus K, Moskalenko V et al. (1997). An abrupt drowning of the Black Sea shelf. Marine Geology 138 (1-2): 119-126.

Sahling H, Bohrmann G, Artemov Y, Bahr A, Brüning M et al. (2009). Vodyanitskii mud volcano, Sorokin trough, Black Sea: geological characterization and quantification of gas bubble streams. Marine and Petroleum Geology 26 (9): 1799-1811.

Sain K, Minshull TA, Singh SC, Hobbs RW (2000). Evidence for a thick free gas layer beneath the bottom simulating reflector in the Makran accretionary prism. Marine Geology 164 (1-2): 3-12.

Satyavani N, Sain K, Lall M, Kumar BJP (2008). Seismic attribute study for gas hydrates in the Andaman Offshore India. Marine Geophysical Researches 29 (3): 167-175.

Shedd W, Boswell R, Frye M, Godfriaux P, Kramer, K (2012). Occurrence and nature of "bottom simulating reflectors" in the northern Gulf of Mexico. Marine and Petroleum Geology 34 (1): 31-40.

Singh S, Minshull TA, Spence G (1993). Velocity structure of a gas hydrate reflector. Science 260 (5105): 204-207.

Sipahioğlu NÖ, Batı Z (2017). Messinian canyons in the Turkish western Black Sea. Geological Society of London Special Publications 464: 365-387.

Sloan ED (1990). Clathrate Hydrates of Natural Gases. New York, NY, USA; Marcel Dekker.

Spadini G, Robinson AG, Cloetingh SAPL (1996). Western versus eastern Black Sea tectonic evolution: pre–rift lithospheric controls on basin formation. Tectonophysics 266 (1-4): 139-154.

Talukder AR, Bialas J, Klaeschen D, Buerk D, Brueckmann W et al. (2007). High-resolution, deep tow, multichannel seismic and sidescan sonar survey of the submarine mounds and associated BSR off Nicaragua pacific margin. Marine Geology 241 (1-4): 33-43.

Taner MT, Koehler F, Sheriff RE (1979). Complex trace analysis. Geophysics 44 (6): 1041-1063.

Tarı E, Şahin M, Barka A, Reilinger R, King RW et al. (2000). Active tectonics of the Black Sea with GPS. Earth, Planets and Space 52: 747-751.

Taylor MH, Dillon WP, Pecher IA (2000). Trapping and migration of methane associated with the gas hydrate stability zone at the Blake Ridge Diapir: new insights from seismic data. Marine Geology 164 (1-2): 79-89.

Vassilev A, Dimitrov L (2002). Spatial and quantity evaluation of the Black Sea gas hydrates. Russian Geology and Geophysics 43 (7): 672-684.

Von Huene R, Pecher IA (1999). Vertical tectonics and the origins of BSRs along the Peru margin. Earth and Planetary Science Letters 166 (1-2): 47-55.

Wang X, Pan D (2017). Application of AVO attribute inversion technology to gas hydrate identification in the Shenhu Area, South China Sea. Marine and Petroleum Geology 80: 23-31.

Woodside JM, Ivanov MK, Limonov AF (1997). Neotectonics and Fluid Flow through Seafloor Sediments in the Eastern Mediterranean and Black Seas, Parts I and II. UNESCO-IOC Technical Series, No. 48. Paris, France: UNESCO.

Woodside JM, Modin DI, Ivanov MK (2003). An enigmatic strong reflector on subbottom profiler records from the Black Sea–the top of shallow gas hydrate deposits. Geo-Marine Letters 23 (3-4): 269-277.

Yanchilina AG, Ryan WB, McManus JF, Dimitrov P, Dimitrov D et al. (2017). Compilation of geophysical, geochronological, and geochemical evidence indicates a rapid Mediterranean-derived submergence of the Black Sea's shelf and subsequent substantial salinification in the early Holocene. Marine Geology 383: 14-34.

Yi BY, Lee GH, Horozal Ş, Yoo DG, Ryu BJ et al. (2011). Qualitative assessment of gas hydrate and gas concentrations from the AVO characteristics of the BSR in the Ulleung Basin, East Sea (Japan Sea). Marine and Petroleum Geology 28 (10): 1953-1966.

Yiğitbaş E, Elmas A, Sefünç A, Özer N (2004). Major neotectonic features of eastern Marmara region, Turkey: development of the Adapazarı-Karasu corridor and its tectonic significance. Geological Journal 39: 179-198.

Zander T, Choi JC, Vanneste M, Berndt C, Dannowski A et al. (2018). Potential impacts of gas hydrate exploitation on slope stability in the Danube deep-sea fan, Black Sea. Marine and Petroleum Geology 92: 1056-1068.

Zillmer M, Flueh ER, Petersen J (2005). Seismic investigation of a bottom simulating reflector and quantification of gas hydrate in the Black Sea. Geophysical Journal International 161 (3): 662-678.

Zonenshain LP, Le Pichon X (1986). Deep basins of the Black Sea and Caspian Sea as remnants of Mesozoic back-arc basins. Tectonophysics 123 (1-4): 181-211.